OPTICA

Atom-based quantum sensing of electromagnetic fields

John Kitching,[1,†,*] James P. Shaffer,[2,7,†] and Dmitry Budker[3,4,5,6,8,†]

[1]Time and Frequency Division, National Institute of Standards and Technology, MS. 847, 325 S. Broadway, Boulder, Colorado 80303, USA
[2]Quantum Valley Ideas Laboratories, 485 Wes Graham Way, Waterloo, Ontario N2L 6R1, Canada
[3]Helmholtz-Institut Mainz, 55099 Mainz, Germany
[4]Johannes Gutenberg-Universität Mainz, 55128 Mainz, Germany
[5]GSI Helmholtzzentrum für Schwerionenforschung GmbH, 64291 Darmstadt, Germany
[6]University of California, Berkeley, Berkeley, California 94720, USA
[7]jshaffer@qvil.ca
[8]budker@uni-mainz.de
[†]These authors contributed equally to this work.
*john.kitching@nist.gov

Received 29 May 2025; revised 17 October 2025; accepted 30 October 2025; published 19 December 2025

The spin and electronic degrees of freedom in atomic systems provide sensitive and versatile means for detecting electromagnetic fields, from DC to THz frequencies, with spatial resolutions ranging from the nanoscale to meter scale. Such sensors offer unique advantages compared to classical approaches, resulting from their intrinsic quantum nature. We review three different sensor modalities: atomic vapor magnetometers, nitrogen-vacancy-center magnetometers, and radio-frequency sensors based on Rydberg atoms. We emphasize the unique features and capabilities of these types of sensors in the context of real-world applications.

https://doi.org/10.1364/OPTICA.569334

1. INTRODUCTION

The measurement of electromagnetic fields is critically important across a broad range of application spaces. The measurement of DC or low-frequency magnetic fields enables the detection of magnetic objects [1,2], geophysical surveying and mapping [3], measurement of biomagnetic fields [4–6], and low-field nuclear magnetic resonance (NMR) [7,8], and extends our understanding of solar radiation and planetary dynamos [9]. Highly localized magnetic field measurements allow high-resolution magnetic imaging [10,11], for example, of integrated circuits [12] or bacteria [13], studies of processes within single living cells [14], the probing of two-dimensional magnetic materials and superconductors [15], and single-spin nuclear magnetic resonance [16]. The detection of RF fields is essential for research and industrial applications in areas such as communications [17], radar [18], and imaging [19]. There are many classical sensor modalities that enable such measurements, but quantum sensors often offer unique advantages.

Atom-based quantum sensors use induced shifts of the energy levels in atomic systems to detect applied electric and magnetic fields [20]. At a basic level, such shifts are determined uniquely by quantum mechanics and fundamental constants of nature such as the fine structure constant and the Bohr magneton. As a result, sensors based on atomic systems typically have excellent long-term frequency stability and can also have intrinsic accuracy, traceable to the Système Internationale (SI). Because individual atoms have a spatial dimension on the order of 0.1 nm, exquisite spatial resolution can be obtained. In addition, weak interaction with the environment, especially for atoms in the vapor phase, implies slow relaxation and correspondingly narrow transition linewidths, leading to high sensitivity.

Quantum mechanics also creates challenges for such sensors. The discrete nature of the measurement process introduces quantization noise that is not present in classical systems composed of a large number of particles. This "quantum projection noise" [21] creates an important limit to the signal-to-noise ratio that can be achieved with a finite number of particles and correspondingly limits the achievable sensitivity.

In this review, we discuss the unique features and particular strengths of atom-based quantum sensors, with an emphasis on how such sensors are used in applications today. It is intended for those unfamiliar with the field of quantum sensing and provides a general introduction to the most basic aspects of quantum sensors such as optical pumping, coherent excitation, and quantum noise. We describe three different quantum sensor modalities as illustrative examples: atomic vapor magnetometers, nitrogen-vacancy centers in solid-state systems, and Rydberg-atom-based sensors of radio-frequency (RF) fields. We discuss the advantages and

limitations of sensors using entanglement and squeezing in atom-based sensors and conclude with an outlook on the future of this field.

2. QUANTUM SENSING

Sensors are used to measure a broad range of quantities including thermodynamic properties (temperature, pressure), fields (electric, magnetic, gravity, optical) and chemical characteristics (composition, molecular structure). Many classical sensing modalities exist typically based on some sort of transduction from the quantity to be measured into an easily detectable output such as voltage or frequency. Most such classical sensors take advantage of bulk or macroscopic properties of materials and are typically subject to thermal noise arising from their coupling to the ambient environment.

By contrast, quantum sensors deal with weakly interacting particles or excitations (or ensembles of such quanta) in which the quantized energy levels are clearly defined. Such particles include atoms, molecules, photons, and phonons. At the microscopic level, the interactions of these particles with each other and with external fields are governed by the laws of quantum mechanics, which include wave–particle duality, superposition, entanglement, and the quantization of energy. Quantum sensing has the same underlying features as the related fields of quantum computing and quantum simulation. In all of these areas, quantum-mechanical particles are prepared in some initial quantum state, they evolve in the presence of a field or other interaction, and the final state is read out giving information about the interaction. In practical realizations of sensors, e.g., Rydberg RF field sensors or atomic magnetometers, two or all three stages can occur concurrently.

For the case of a two-level quantum system, these processes are commonly visualized using the Bloch sphere representation [22,23], as shown in Fig. 1. The quantum-mechanical state $|\psi\rangle$ of a two-level atom can be parameterized by two angles θ and ϕ as $|\psi\rangle = \cos(\theta/2)|1\rangle + \sin(\theta/2)e^{i\phi}|2\rangle$. Any such state can be represented as a unit vector on the Bloch sphere with the polar angle given by θ and azimuthal angle given by ϕ, as shown in Fig. 1(a). The sensing sequence begins with a state preparation step, in which the atom is prepared in a specific quantum state sensitive to the field to be measured, Fig. 1(b). After state preparation, the evolution for a field applied along the system quantization axis, Fig. 1(c), is given by

$$\phi(t) = \frac{1}{\hbar}\int_0^t H_{\rm int}\mathrm{d}t, \tag{1}$$

where $H_{\rm int}(\boldsymbol{\mu},\boldsymbol{\mathcal{F}})$ is the Hamiltonian governing the interaction of the atomic degree of freedom $\boldsymbol{\mu}$ with the field $\boldsymbol{\mathcal{F}}$. After some time T, the newly evolved state of the atom is measured, Fig. 1(d), to determine ϕ, from which the field $\boldsymbol{\mathcal{F}}$ is deduced. Atomic ensembles are well-suited to high-performance sensing because typically the response of the atomic energy levels to an applied field is determined by quantum mechanics and fundamental constants of nature. For example, the shift of the ground-state Zeeman levels in an atom due to an applied magnetic field $\mathcal{F} = B$ is given (to first order) by

$$\Delta E_L = \frac{\hbar e g}{2m_e}B, \tag{2}$$

where e is the charge on the electron, m_e is the electron mass, and g is the g-factor of the atom. This means that to the extent that the atomic ensemble is isolated from all perturbing effects other than the measured field, any atom of a given species will always give the same response to an applied field. Sensors based on atomic systems therefore fundamentally embody traceability to the Système Internationale (SI) and typically also have associated advantages such as good long-term stability and repeatability.

State preparation is typically accomplished through optical pumping [24]. For example, atoms can be spin-polarized through illumination by polarized light [see Fig. 2(a)] or can be prepared in unique hyperfine energy levels using light tuned to specific frequencies [Fig. 2(b)]. In each of these cases, atoms in states that couple to the optical fields are excited into the upper energy level. Subsequent decay can be either to the original level (in which case the atom is eventually excited again) or to an uncoupled level. Since the uncoupled level does not interact with the optical field, atomic population accumulates in this level, thereby preparing the atomic state.

Not all state preparation involves optical pumping directly. In Fig. 2(c), an electromagnetically induced transparency (EIT) system is depicted. The EIT phenomena can be interpreted as an interference between absorption on the probe laser transition and a coherent upward and downward coupling laser transition [25]. These processes are π out of phase with each other so when their

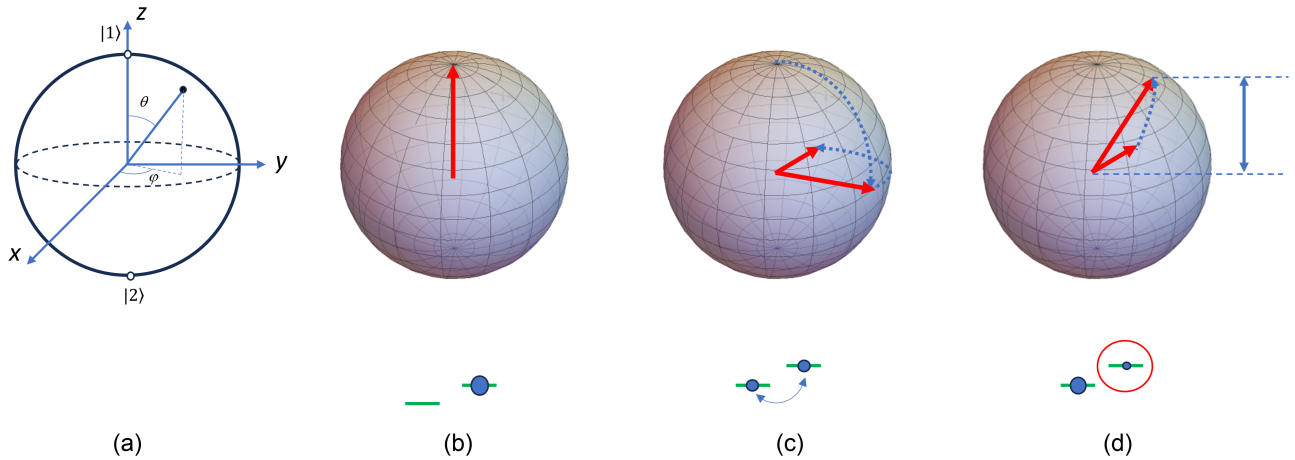

Fig. 1. Bloch sphere representation of a two-level quantum system quantum sensor. (a) Representation of a two-level atomic system in terms of parameters θ and ϕ; (b) initial state preparation; (c) evolution in the presence of a field; (d) final state detection.

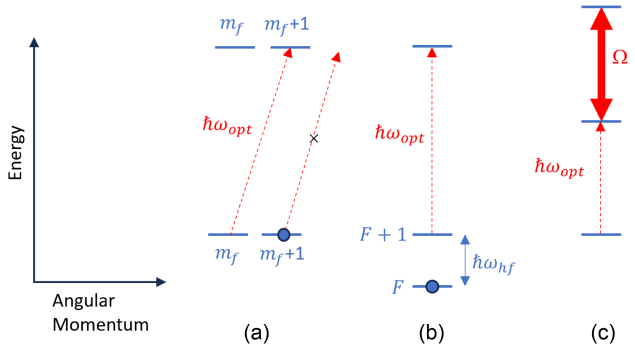

Fig. 2. Optical fields at ω_{opt} pump atoms into uncoupled states. (a) Spin polarization of atomic systems using circularly polarized light. Circularly polarized photons add angular momentum to the atoms when absorbed and preferentially populate certain angular momentum states (here $m_f + 1$). (b) Light tuned to a specific frequency resonant with one hyperfine level (here $F + 1$) pumps atoms into the uncoupled hyperfine level (F). (c) An EIT ladder scheme typically used to excite Rydberg states.

amplitudes are added, they can reduce the absorption of the probe laser. In EIT, a pair of resonant optical fields (coupling and probe lasers) puts the atoms into a coherent superposition of states that is transparent to the combined optical field. Practically, setting up EIT in an atom involves consideration of optical pumping for two principal reasons. First, to increase the coherence time and available atoms, it is advantageous to work on transitions that decrease decay out of the target system of energy levels. Likewise, it is desirable to pump the maximum number of atoms into the target system of energy levels, provided that collisional dephasing is negligible. Second, the polarizations of the probe and coupling lasers set the distribution of magnetic sublevels and hyperfine states in the Rydberg state. By manipulating those populations, the sensor can be designed so that it is sensitive to polarization [26].

The coherent evolution of the atom–field interaction occurs in the presence of relaxation from a variety of physical processes. Dephasing and decay can occur due to effects such as radiative emission, collisions, transit time through the sensor, and laser noise. Radiative relaxation results from spontaneous emission of light from an excited state. Collisional relaxation occurs when atoms interact with other atoms, the matrix in which the defects are contained (phonon relaxation), or the walls of a vapor cell. Understanding of relaxation mechanisms is important in order to optimize a sensor. Generally, the longer the time that the sensor can be influenced by the external field without perturbation, the more sensitive the measurement can be. The dephasing and decay mechanisms of the sensor fundamentally limit the sensitivity along with the constants that determine the response of the sensor to the electromagnetic field, i.e., the quality factor of the measurement system and the fundamental signal-to-noise ratio.

A considerable amount of work over many decades has been focused on reducing the effects of relaxation. Buffer gases and wall coatings have been developed to reduce wall-induced relaxation [24] and Doppler broadening [27] of atomic spins in the vapor phase. To achieve similar objectives, laser cooling and trapping techniques [28,29] allow one to slow and hold atoms for extended periods without coming into contact with the container walls, while spin-echo techniques [30] suppress inhomogeneous relaxation arising due to magnetic field gradients.

3. EXAMPLES OF QUANTUM SENSING MODALITIES

When comparing different sensors, there is no single universal characteristic—each application has its own requirements. While sensitivity is most common, a plethora of other metrics can be important, including spatial resolution, bandwidth, accuracy, dynamic range, dead zones, errors due to changes in orientation (heading errors), and ease of implementation. In the following, we discuss three different quantum sensing modalities: atomic vapor magnetometers, nitrogen-vacancy (NV)-center magnetometers, and RF electric field sensors based on Rydberg atoms.

A. Atomic Vapor Magnetometers

Atomic vapor magnetometers are based on the Larmor precession of atomic spins in a magnetic field. The underlying physics has its origins in the work of Hanle [31], who discovered that the polarization of the light emitted from an atomic ensemble undergoing resonance fluorescence depended on the applied magnetic field. In 1957, it was pointed out [32,33] that the precession of an ensemble of optically pumped alkali atoms in a magnetic field could be measured optically by detecting the modulated power of light transmitted through the ensemble. These ideas led to the rapid development of optical atomic magnetometry throughout the late 1950s and early 1960s [34–38]. By 1961, an alkali vapor magnetometer had even been flown in space [39]. Previous reviews of atomic magnetometers can be found in Refs. [4,40–43]

These early magnetometers were based on an optical measurement of the transverse or longitudinal component of the atomic polarization precessing in the magnetic field, driven by an applied RF field, as shown in Fig. 3. Atoms were spin-polarized (state preparation) through illumination with circularly polarized light, and their precession (coherent evolution) about the magnetic field was driven by an applied RF field at the Larmor frequency. The transverse (M_x) or longitudinal (M_z) component of the polarization (with respect to the magnetic field) was then detected using the AC or DC components of the polarizing field absorption; see Fig. 3(a). M_x magnetometers [44] are now well-developed commercially and are widely used in applications such as geophysical surveying due to their high bandwidth and simple implementation. M_z magnetometers typically have higher accuracy and lower heading error [45] but typically suffer from reduced bandwidth.

Precession of atomic spins can also be driven optically [46], through modulation of the optical pumping field at either the Larmor frequency [47] (often referred to as a Bell–Bloom magnetometer) or the hyperfine frequency [48–50], as illustrated in Fig. 3(b). In essence, the low-frequency coherences in the atoms are excited through the mixing of two or more optical frequencies via the nonlinearity of the atomic response. For these sensors, no applied oscillating magnetic fields are needed to drive the spin precession. This allows, for example, standoff, or remote magnetometry [51–55] as well as improved long-term stability for use in space applications [56,57].

Magnetometers based on ^{4}He excited with an RF discharge into a metastable state [58–60] operate in a similar manner to alkali magnetometers. Since the ^{4}He nucleus has no spin or magnetic moment, heading errors are reduced, and higher accuracy can be obtained than is typical in alkali magnetometers. It is for this reason that ^{4}He magnetometers are often flown in space [61,62]. The precession of the nuclear spin of ^{3}He (or other noble gases such

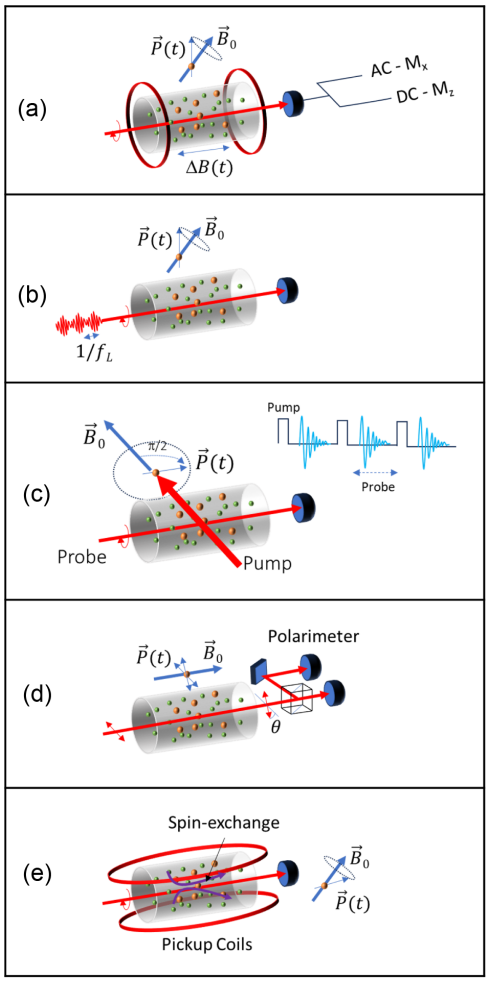

Fig. 3. Atomic magnetometers. $\vec{B}_0$ represents the field to be measured, and $\vec{P}(t)$ indicates the atomic polarization. (a) M_x and M_z magnetometers. (b) Bell–Bloom magnetometer. (c) Free-decay magnetometer. (d) Magneto-optical-rotation magnetometer. (e) Nuclear spin magnetometer polarized via spin exchange with optically pumped atoms.

as Kr and Xe) can also be used for magnetometry, typically polarized via spin-exchange [63] with a co-located optically pumped alkali species. The weak interaction of nuclear spins with the environment implies relaxation times as long as many hours and correspondingly higher resonance quality factors. ^{3}He magnetometers have the best sensitivity of any magnetometer at low frequencies [64] but also have low bandwidth.

The stability of atomic magnetometers is often limited by vector and tensor AC Stark shifts [65–67] arising from the optical fields used to optically pump (polarize) and probe the atoms [68,69]. Such shifts can be suppressed through the use of linearly polarized light in optically driven magnetometers [70], diffusive atom transport [71], and spatial averaging in wall-coated cells [72]. Alternatively, the magnetometer can be operated in a pulsed mode as shown in Fig. 3(c). Here the atoms are spin-polarized with a short pulse of strong optical pumping light. The subsequent precession in the magnetic field is monitored with a weak probe beam which only minimally perturbs the atomic energy levels. Such magnetometers can be combined with quantum-nondemolition measurements of the spins [73] using a detuned probe to achieve high sensitivity [74,75] and high bandwidth [76]. AC Stark shifts can also be useful for suppressing the unwanted effects of nonlinear Zeeman shifts [77], for implementing magnetometry with RF driving without actual RF fields [78], and to convert a scalar magnetometer into a vector magnetometer [79].

In order to achieve high signal-to-noise ratios, it is useful to operate the vapor cell at elevated temperatures (typically 100°C–200°C). Here, the high vapor density leads to strong relaxation due to spin-exchange collisions [80,81]. At low magnetic fields, such that the spin precession frequency is smaller than the collisional relaxation rate, it was discovered that spin-exchange relaxation can be strongly suppressed [82,83]. This spin-exchange-relaxation-free (SERF) mode [84] can be used to great advantage for high-precision magnetometry [85,86], allowing for sensitivities as low as 160 $\mathrm{aT}/\sqrt{\mathrm{Hz}}$ [87]. Because the Larmor precession frequency must be small, operation in the Earth's magnetic field is usually not possible with this type of magnetometer without additional elements such as compensation coils.

Highly miniaturized "chip-scale" magnetometers [88,89] have been developed for which the vapor cells are fabricated using silicon micromachining techniques [90–92]. Total field magnetometers with a sensitivity better than 100 $\mathrm{fT}/\sqrt{\mathrm{Hz}}$ at 10 Hz have been demonstrated [93], while sensitivities of 20 $\mathrm{fT}/\sqrt{\mathrm{Hz}}$ have been achieved in the SERF regime with such cells [94]. Figure 4 shows the sensitivity as a function of measurement frequency for a number of atomic vapor magnetometers compared to fluxgate magnetometers, search coils and superconducting quantum interference device (SQUID) magnetometers.

Laser cooled and trapped atoms including Bose–Einstein condensates are another interesting platform for magnetometry, as reviewed in [105]. While not as practical as other types of magnetometers, these devices find application as comagnetometers in fundamental physics experiments [106], as sensors of surface magnetism [107–110], and as part of cold-atom multisensor platforms on board spacecraft [111].

In addition to sensitivity, there are many other important properties that characterize atomic magnetometers. These include accuracy, bandwidth, dead zones, dynamic range, heading error, and whether the sensor measures the field magnitude (scalar) or the field along a specific direction (vector). These properties are illustrated for each sensor type in Table 1. Vapor cell magnetometers are used in geophysical surveying [3,45], magnetic anomaly detection [1], navigation [112], biomedical imaging [113,114], space science [9,115], and fundamental physics [116].

B. NV-Center Magnetometers

Since the late 2000s, one of the rapidly developing sensor platforms has been color-center defects in crystalline materials such as diamond, silicon carbide, and hexagonal boron nitride. Of these, the most widely used are the nitrogen-vacancy (NV) centers in diamond. An NV center is comprised of a substitutional nitrogen atom and an unfilled vacancy in adjacent sites in the diamond crystal. NV centers may exist in various charge states; the one primarily used for sensing is the singly negatively charged NV^-, which has electron spin $S = 1$ in the ground state.

With its relatively simple "atom-like" energy-level structure (Fig. 5), NV centers have a set of remarkable properties that make them attractive for sensing applications, from DC [121] to RF [122]. First, it is easy to polarize the centers, and hence implement the initial state preparation step. Typically, this is done by shining

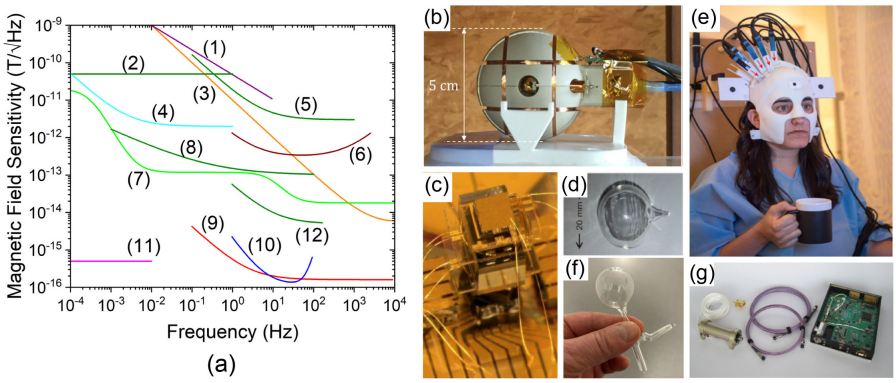

Fig. 4. (a) Field sensitivity as a function of frequency. (1) space fluxgate [95]; (2) space CPT [56]; (3) search coil [96]; (4) atomic NMOR [97]; (5) ^{4}He [98]; (6) microfabricated M_x [93]; (7) pulsed nonlinear magneto-optic rotation [99]; (8) Mx, adapted from [100]; (9) SQUID [101]; (10) cm scale SERF [87]; (11) ^{3}He nuclear magnetic resonance (NMR) [64]; and (12) microfabricated SERF [102]. (b) ^{4}He magnetometer developed for space. Reproduced from Ref. [98], with permission of AIP Publishing. (c) Chip-scale M_x magnetometer. Reproduced from Ref. [89], with permission of AIP Publishing. (d) Vapor cell for a ^{3}He magnetometer. Reproduced from Ref. [103] with permission from Springer Nature. (e) Compact SERF magnetometers being used for biomagnetic measurements. Reproduced from Ref. [104] with permission from Springer Nature. (f) Wall-coated vapor cell used for NMOR. (g) CPT magnetometer developed for space. Reproduced from Ref. [56] under CC-BY 3.0.

Table 1. Properties of Various Vapor Cell Atomic Magnetometers[a]

	Vector/Scalar[b]	Bandwidth (Hz)	Dead Zones	Dynamic Range	Heading Error	Accuracy nT[c]	Reference
M_x	Scalar	100	P, A[d]	>100 nT	1 nT	2	[44]
M_z	Scalar	10	P, A[d]	>100 nT	0.05 nT	0.1	[44]
CPT	Scalar	100	*P*	>100 nT			[117]
^{4}He	Scalar	100	None	>100 nT	<0.05 nT	0.05	[60]
^{3}He	Scalar	0.01	Design dependent	>0.1 T	Design dependent	0.0001[d]	[103]
SERF	Vector	100	N/A[e]	<10 nT	N/A[f]		[85]
NMOR	Scalar	1000	Design dependent[g]	100 μT	Design dependent[g]		[118]
Pulsed FID	Scalar	100	*P*	>100 nT			[74]
Chip-scale M_x	Scalar	1000	P, A[d]	>1 μT	10 nT[h]	20[g]	[119]
Chip-scale SERF	Vector	100	N/A[f]	<100 nT	N/A[f]		[94]

[a]P indicates a polar dead zone, and A indicates an azimuthal dead zone. NMOR refers to magnetometer based on nonlinear magneto-optic rotation, and FID refers to magnetometers based on free induction decay.

[b]This column refers to the fundamental nature of the sensor. Any scalar sensor can be straightforwardly converted into a vector sensor, for example, through addition of a static or dynamic magnetic field.

[c]In a field of 50 μT.

[d]Assumes single pump–probe beam and RF coil axis collinear with optical field axis; see Fig. 3.

[e]At 0.1 T.

[f]Vector sensors are sensitive along a single axis and hence do not have dead zones or heading errors.

[g]See, for example, [120].

[h]Extrapolated from conventional large-scale M_x magnetometers.

light from a green (e.g., 515–532 nm) laser or light-emitting diode onto the diamond. While optical transitions in the NV centers are largely independent of the spin state, the excited centers either decay back to the ground state or undergo *intersystem crossing* to singlets [123]; the latter process occurs due to spin–orbit interaction. The result is that a large fraction of NV centers are initialized into the ground $m_s = 0$ Zeeman sublevel, independent of the light polarization. Encoding of the field information on the phase of the atomic coherence is caused by the dependence of the energies of the ground-state sublevels on magnetic and electric field, temperature, or strain. Finally, the readout stage can also be done optically because laser-induced photoluminescence, absorption, and photoionization of the NV center depend on the spin state. This is due to similar mechanisms that create the initial polarization. For example, if the NV center is in one of the $m_s = \pm 1$ states, it has a significant chance of decaying to singlets, which leads to increase of the population of the metastable lower singlet and enhanced absorption on the 1042 nm transition between the singlet states. This readout technique works well for dense NV ensembles: see, for example, Ref. [124] and references therein.

There are several features that make color-center sensors, and specifically NV diamond, particularly attractive in a host of applications. The primary factor is a combination of high sensitivity

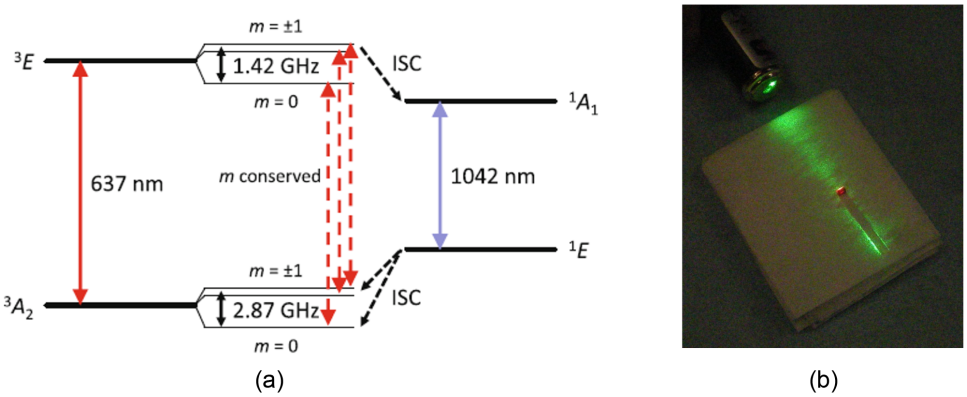

Fig. 5. (a) Electronic energy levels and transitions in negatively charged NV centers in diamond. ISC: intersystem crossing. This level structure is relevant for room temperature sensors; at cryogenic temperatures, the level structure is more complex [123]. Reproduced from [125] with permission from Springer Nature. (b) Photograph of a diamond sample with a large (several parts per million) relative concentration of NV centers illuminated with green light and fluorescing in the red.

[126] with high spatial resolution, down to atomic scale [121]. Important secondary features include the implementation in a solid-state platform capable of operating in a wide temperature range—from deep cryogenics to several hundred kelvin—and multisensing capabilities (i.e., an ability to combine sensing of different parameters in a single device). Nanoscale sensing with a single color center as a sensor is in itself a rapidly developing subfield. A single NV center used for sensing may be located within several nanometers from the surface of a bulk diamond with low concentration of impurities could be incorporated within a nanodiamond, or be part of a scanning probe; see, for example, [127] and references therein.

Table 2 summarizes some of the state-of-the-art results for various current sensing configurations, although major advances are made in this field every year or two. The table shows sensitivities for both single-NV configurations enabling measurements with nanoscale resolution, as well as ensemble-NV configurations where typical sensing volumes are on the order of $10^4 - 10^6$ μm^3 or significantly larger when ferromagnetic flux concentrators are used. Such concentrators allow boosting of the sensitivity by several orders of magnitude at the expense of a larger sensor volume and increased low-frequency noise [130].

The sensitivity of a magnetic sensor typically scales as the square root of the spin-relaxation rate (or, equivalently, $1/\sqrt{T_2}$ where T_2 is the transverse relaxation time). This rate can often be greatly reduced by dynamical decoupling techniques [135]. In the simplest case, this is spin echo (a.k.a. Hahn echo) and its various generalizations, often to sophisticated sequences of multiple pulses; see, for example, [136]. In Ref. [136], the sample is cooled to a liquid nitrogen temperature to avoid the effective T_2 time from being limited by the longitudinal relaxation time T_1, which is longer when the sample is cooled (due to the suppression of phonon-related relaxation). While dynamical decoupling generally boosts the sensitivity, it often requires synchronization of the pulses with the measured signal and so can limit the measurement to cases where the frequency of the signal is known or the relative frequencies can be scanned to synchronize the measurement and signal to obtain the spectrum of the signal. The last line in Table 2 shows the sensitivity of a sensor that detects changes in a microwave field via a change in the Rabi oscillations between energy levels of NV centers driven by this field [134].

Some promising applications of NV-center magnetometry include the study of high-temperature superconductors [137], magnetocardiography [138], detection of chemical radicals [139], and nanoscale nuclear magnetic resonance [16].

C. Rydberg Atom Sensors

Rydberg atom sensors can be classified as a quantum technology because they use the discrete nature of atomic energy levels, including their stability, and quantum interference between them. For a more detailed discussion of Rydberg atom RF sensors and a more thorough survey of the literature, the reader is referred to reviews

Table 2. Some of the Currently Most Sensitive Magnetometers Based on NV Centers in Diamond[a]

Sensor	Sensitivity	Features	References
Single NV	$9\ \mathrm{nT}/\sqrt{\mathrm{Hz}}$	AC (0.5–1.3 kHz) with Hahn echo	[128]
Single NV	$0.5\ \mathrm{nT}/\sqrt{\mathrm{Hz}}$	kHz–MHz, with DD, bias field of 0.8 T	[129]
Ensemble	$0.9\ \mathrm{pT}\cdot\sqrt{\mathrm{s}}$	DC–1 kHz; FC	[130]
Ensemble	$0.21 - 0.46\ \mathrm{pT}\cdot\sqrt{\mathrm{s}}$	DC and AC (1–10 kHz), DD, no FC	[131]
Ensemble	$195\ \mathrm{fT}/\sqrt{\mathrm{Hz}}$	DC to 300 Hz, no DD, FC	[132]
Ensemble	$70\ \mathrm{fT}\cdot\sqrt{\mathrm{s}}$	AC (70 kHz–3.6 MHz), DD, FC	[133]
Ensemble	$3.4\ \mathrm{pT}/\sqrt{\mathrm{Hz}}$	Microwave (~ 3 GHz)	[134]

[a]DD–dynamical decoupling; FC–magnetic flux concentrators. The sensitivity is quoted in units used in original references. There is a numerical factor (typically, $\sqrt{2}$) to go from $\mathrm{pT}\cdot\sqrt{\mathrm{s}}$ to $\mathrm{pT}/\sqrt{\mathrm{Hz}}$ [105]. All listed results were obtained with room-temperature sensors, with the diamond temperature generally higher due to laser-light heating.

that focus solely on Rydberg atom RF sensors [140–145]. The quantum features of Rydberg atom RF sensors are used to detect and measure classical RF electromagnetic fields. Rydberg states are useful for RF field sensing because the transitions between these high-lying levels in an atom are in the RF range, have large transition dipole moments, and span a large range of frequencies ranging from DC to THz compared to valence states of atoms or molecules. The resonant enhancement offered by the Rydberg transitions promises to make these sensors competitively sensitive when compared to antenna based systems. Although not yet demonstrated, increasing the sensitivity to reach the thermal limit of classical antennas is an intense area of current research. At present, the sensitivity limits for all-optical sensing [146] and for RF heterodyne measurements [147–149] are around 1 $\mu Vm^{-1}Hz^{-1/2}$. These numbers are similar to classical approaches, but must improve by an order of magnitude in the electric field sensitivity to reach, or significantly surpass, the thermal limit of antenna-based systems.

Rydberg atom sensors work by dressing the atom with laser fields so that the absorption of a "probe" laser changes in the presence of an RF electromagnetic field as shown in Fig. 6. The lasers typically form an electromagnetically induced transparency (EIT) [155] or electromagnetically induced absorption (EIA) system that is modulated by the dressing RF field to be sensed, as shown by the Autler–Townes splitting in Fig. 6(c). Several schemes have been explored, but two key common aspects are coherent response of the atoms to an RF wave, and relative insensitivity to a thermal field [156–158]. The properties of the RF field are derived from the scattering of probe laser photons out of the optical mode, while the absorption and scattering of the RF electromagnetic field are small. Typically, the sensitivity of a Rydberg atom sensor is limited by the shot noise of the probe laser light. The large collisional cross sections between Rydberg atoms limit the Rydberg state populations and hence the ability to increase the probe laser power to increase the signal to noise. As the probe laser intensity increases relative to the decay rate of the probe laser transition, the Rydberg population grows, increasing the density of the Rydberg atoms and hence the dephasing rate due to collisions. Thermal noise can affect the sensor through its influence on the decay rates of the Rydberg states involved in sensing the RF electromagnetic field, referred to as black body effects [156–158].

In the normal operating mode of these sensors, the polarization, evolution, and probing typically occur concurrently in order to facilitate continuous measurement of the RF field, although time-dependent measurements conforming to the separation of these stages have been investigated in the laboratory [159]. Normally, the atom is always under the influence of the state preparation lasers, while the amount of absorption experienced by the probe laser light is continuously monitored to enable applications, where sensing pulsed RF fields is critical, and maximum-bandwidth readout is desired. The transient response to changes in the RF electromagnetic field can be limited by the response time of the dressed atomic system, favoring probe transitions with larger scattering rates, i.e., the D1 and D2 transitions of alkali atoms as opposed to a weaker atomic transition.

Variants of the approach shown in Fig. 6 have been developed. Multiple (i.e., >2) coupling lasers have been used to avoid wavelengths that are difficult to produce and eliminate residual Doppler broadening of the EIT/EIA feature [146–149,151–153]. Fluorescence has also been used to extract the properties of the RF field [154]. One of the most significant variants is the use of an RF heterodyning field near resonance with the Rydberg transition frequency. The heterodyne RF field is used to induce Autler–Townes splitting and detect changes due to the incident RF wave, linearizing the response to low amplitude RF fields and providing a modulation for detecting a beat-note [147,148]. The latter approach requires a separate local RF source and antenna to apply the auxiliary RF field.

Rydberg atomic RF sensors have several advantages over classical RF sensors, particularly those that require an antenna to convert an over-the-air RF electromagnetic wave into an electrical signal (See Table 3). Rydberg atom RF sensors have an extraordinarily high carrier bandwidth since their response can be tuned

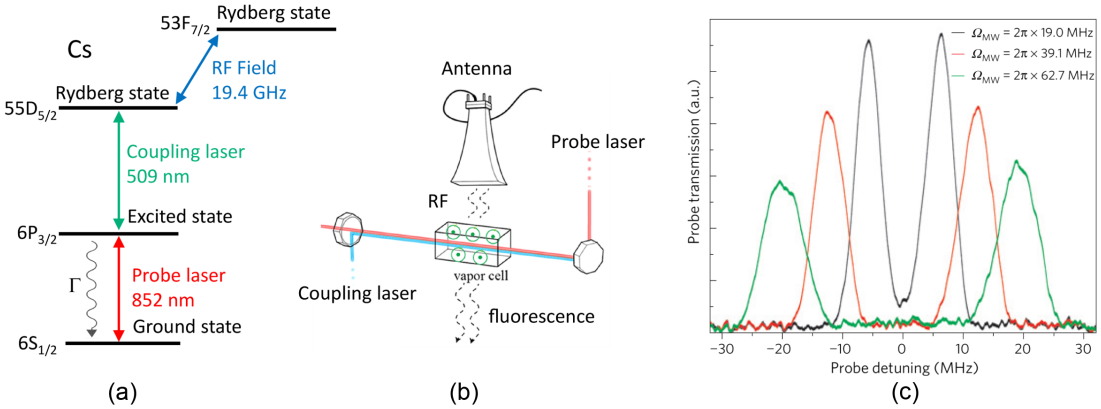

Fig. 6. (a) Typical approach to Rydberg atom sensing. Variants differ in the number of coupling lasers and whether or not an auxiliary RF field is used on the RF transition [146–153]. Reasons for the variants include the availability of high quality, inexpensive lasers, Doppler cancellation, and signal processing. The probe laser transmission through a vapor cell is monitored to derive the properties of the RF field [150]. In some cases, fluorescence from a state in the system has been used to obtain the properties of the RF field [154]. The decay rates of the Rydberg states are typically small compared to the Rabi frequency of the coupling laser as well as the RF field that is detected, i.e., the coherence parameter for the transitions is $\gg 1$. It is important that the spectroscopic technique is sub-Doppler, in order to get high spectral resolution. In the scheme, shown in (a), the lower three levels form an electromagnetically induced transparency (EIT) system that yields a narrow transmission feature through the atomic sample. In the absence of the RF field, the EIT system is interferometer where the absorption of the probe laser cancels due to the absorption and emission processes enabled by the two lasers. The RF field modulates the EIT process, i.e., the probe transmission, by dressing the two Rydberg states. Electromagnetically induced absorption (EIA) in other laser configurations is used in the same qualitative way [146,149,151,152]. (b) An abstraction of the key elements of a Rydberg atom RF sensor. (c) Autler–Townes splitting of the EIT resonance induced by the presence of an RF field. From Ref. [150].

Table 3. Some Advantages and Unique Features of Rydberg Atom RF Sensors

Property	Explanation and Advantages
Large carrier bandwidth	The same sensor can, in principle, detect signals from DC to THz frequencies, depending on the Rydberg state RF transitions that are available. To measure across this bandwidth requires tuning a laser, but there are no equipment changes like those required for conventional antenna-based systems
Self-calibration	In the regime where an Autler–Townes splitting is measured, the splitting depends directly in the strength of the field, its polarization, and the transition dipole moments of the states involved. The RF field can be measured against a stable atomic system.
Dielectric sensors	The sensors can be made without metal so they can be more electromagnetically transparent enabling operation in the near field of a device under test.
High spatial resolution	The sensors are atoms, albeit with RF absorption cross sections depending on the wavelength, so the physical size of the sensor can be smaller than the RF wavelength.
Passive sensors	The sensors do not generate significant RF radiation since the decay rates on the RF transitions are small.
High accuracy and repeatability	The potential accuracy and repeatability are high because of the fundamental nature of the atomic system.
Signals are read out at baseband	The modulation of carrier wave used to transmit information is directly read out from the photodetector. As a consequence, mixers and high-bandwidth ADCs are not required to transfer the signal to digital signal processing.
Fast and agile frequency scanning	The sensing frequency can be changed as fast as the coupling laser can be tuned to reach different Rydberg states (<1 μs) [167]. Coupled with large carrier bandwidth (no equipment changes) and arrays of vapor cells, extremely dynamic and adaptive RF sensing is possible in a compact system.

from near DC to the THz range. Here, we note that the carrier bandwidth is the frequency range over which the sensor can be tuned using the coupling laser, while the instantaneous bandwidth is the response time of the sensor. No single conventional RF system exists today that can tune over this range of frequencies without antenna and equipment changes. In conventional RF technology, most antennas are made from metal and are used in the far-field where their interaction with a device under test is minimal. ETSI-3GPP standards [160,161] for testing 5G communications equipment are largely based on the assumption of far-field testing, which becomes prohibitive since the distance required scales like D/λ^2, where D is the device aperture, and λ is the wavelength. Many modern, high-frequency (>24 GHz) antennas designed for beam forming have large apertures. Hence, for large antenna apertures, and higher frequencies, the far-field distance becomes problematic. Rydberg atom sensors can be made from entirely dielectric materials and can be engineered for high RF transparency and low-radar cross section [162–165] and therefore can be used effectively in both the near-field and Fresnel zones. Unlike conventional RF antenna-based detection, Rydberg atom sensors are read out at baseband. As a consequence, mixers and high-speed analog-to-digital converters (ADCs) are not required to transition signals into digital signal processing. Rydberg sensors are also unique because their fundamental physical size is the atom. The sensors can be made with subwavelength dimensions and can image RF fields at subwavelength length scales. It is important to note that the RF absorption cross-sectional scales with the wavelength, i.e., the effective antenna aperture for each atom is the absorption cross section of the RF atomic transition. In addition, readout is accomplished photonically as the signals are carried to and from the sensor optically. The signals are immune to RF noise and overcome the challenges of RF cabling at high frequencies (>24 GHz—so-called FR2 bands). Finally, Rydberg atom sensors can be self-calibrated when the RF signal is measured in the Autler–Townes regime [140,142–145,166,167]. Rydberg atom sensors therefore have the potential to link RF power measurements to atomic constants and hence achieve accuracy and SI traceability. In many cases, these Rydberg atom sensors have advantages over classical approaches in size, weight, power, and cost, because they can sense over a very wide frequency range without the use of mixers, auxiliary RF sources, multiple antennas, high-cost cabling, etc.

Rydberg atom sensors have some notable limitations, some of which we point out here. The most notable limitations are that the best instantaneous bandwidths that have been achieved are on the order of 10 MHz, although it is possible to detect a larger bandwidth signal if the incoming signal is known and is using a sufficient Hamming distance, e.g., M-sequences or Gold codes [168]. Another disadvantage is that off-resonant sensing reduces sensitivity, which at this time is not as high as the best classical RF equipment. Finally, the fabrication of vapor cells for RF sensors is complicated by the fragility of the Rydberg states that are used [162–165]. Collisions with background gases and electric fields from the vapor cell surfaces disturb the atoms and result in homogeneous and inhomogeneous broadening of probe laser transmission. Stark shifts can mix the Rydberg states reducing the accuracy of the sensors. Work is currently being carried out to optimize and engineer vapor cells for Rydberg atom sensing [169–172].

Taking into account both the advantages and disadvantages, Rydberg atom sensors can have an impact in test and measurement of antennas and RF devices, particularly those operating in the FR2 bands. Radar is another area where Rydberg atom sensors can make an impact, since many radar applications do not require large instantaneous bandwidths, but benefit from multifrequency operation [173]. Both of these areas are broad, and one can envision applications that cannot be done with what is available today with standard RF equipment. There may be niche applications in communications, such as compact, low-frequency systems, where the price of low instantaneous bandwidth can be tolerated. We note

that the low instantaneous bandwidth can be partially compensated by the ability of the same back-end system to drive multiple sensors detecting at multiple frequencies in order to increase the data rate.

D. Comparison of Sensing Modalities

The sensor modalities described above have unique features that make them well-suited to certain applications. Vapor cell magnetometers currently achieve (along with SQUID magnetometers) the best sensitivity to DC fields, well below 1 fT/$\sqrt{\text{Hz}}$. Due to their small physical size and proximity to magnetic sources, NV-center magnetometers have particular strengths for sub-mm magnetic imaging and the detection of very small dipole moments. Rydberg atom sensors are well-suited to the detection of RF fields from MHz frequencies to the THz range.

4. ENTANGLEMENT AND SQUEEZING

In many cases, atom-based quantum sensors that are photonically prepared and read out are limited by the fundamental noise in the optical fields and discrete nature of the atoms. Laser-generated fields are coherent superpositions of photon number states and possess associated intensity and phase fluctuations, the so-called photon shot noise. The atoms that are used for sensing are discrete, with quantized energy levels, leading to projection noise and atom number fluctuations, such as those associated with atoms transiting through the laser beams. One way to overcome these types of noise is through engineering of the fields and the method by which the atoms are prepared, i.e., squeezing and entanglement. The disadvantage of using squeezing and entanglement is that these phenomena require additional resources and systems that can make implementation in real-world applications unattractive or even prohibitive. The methods needed to produce entanglement and squeezing can be complicated and difficult to implement. It is far more straightforward to reduce the photon and atom shot noise by using more atoms and photons. There are conditions where the number of participating atoms and photons cannot be increased. Examples are biological samples that can be damaged by intense light fields and Rydberg atom sensors where, for fixed atom–laser interaction volumes, the practical density of the atoms is limited by Rydberg atom collision rates.

A fundamental aspect of quantum mechanics is the discrete nature of energy levels in quantum systems. In classical mechanics, energy is a continuous quantity and hence can in principle be measured with arbitrary precision. Quantization of energy introduces a "counting error" that in effect adds noise to any measurement of the system energy. This is known as the Heisenberg limit: for a system of N particles (atoms or photons) in a state with energy E, quantization implies that the energy can be measured with at best a resolution of

$$\delta E \simeq \frac{\hbar}{TN}, \tag{3}$$

where $\hbar$ is the reduced Planck's constant, and T is the relaxation or measurement time.

The Heisenberg limit can only be attained for $N > 1$ through particle entanglement or squeezing. For quantum-mechanically uncorrelated particles, a second limit applies, known as the standard quantum limit (SQL):

$$\delta E \simeq \frac{\hbar}{T\sqrt{NM}} = \frac{\hbar}{\sqrt{NT\tau}}, \tag{4}$$

where τ is the total time over which $M = \tau/T$ independent measurements are made on each particle. Intuitively, this can be thought of as the statistical counting error of a randomly distributed set of N events measured over a time T. From Eqs. (3) and (4) above, it is clear that for large numbers of particles ($N \gg 1$), a substantial improvement in energy resolution (and hence field sensitivity) can be gained through the use of squeezing and entanglement.

Over 10 dB of squeezing (a factor of 10 reduction in the noise compared to the SQL) has been obtained for both optical fields [174] and spins [175,176], which in principle allows for meaningful improvements in sensor performance. Such improvements have been realized experimentally in optical interferometry [177,178], atomic clocks [175,179,180], atom interferometers [181,182], and vapor cell magnetometers [76]. Spin-squeezed optical clocks now show clear metrological gain as verified by frequency comparison measurements [183].

The improvement gained through the use of quantum resources is intimately connected with the constraints placed on the system. For example, if the number of particles is allowed to vary, a resolution equivalent to the Heisenberg limit for N particles can be obtained without quantum correlations (SQL) by using N^2 particles. It has been noted [184,185] that in the presence of decoherence, the ultimate resolution of a frequency measurement is the same for both correlated and uncorrelated atoms, but that quantum correlations allow faster extraction of information from the atomic ensemble. This allows for higher-bandwidth sensing [76] and relaxes the constraints on the stability of local oscillators in atomic clocks [186]. Another important consideration is the fragility of quantum states to loss and relaxation. Even modest levels of dissipation result in the almost complete elimination of the metrological advantages gained by the use of quantum correlations, and great care must be taken to avoid such effects. This can be particularly challenging in real-world environments.

Quantum nondemolition and back-action evading measurement strategies [187] allow one spin variable (e.g., J_z) in an atomic ensemble to be measured with the quantum-mechanical back-action from the measurement affecting only an orthogonal spin degree of freedom (J_x and J_y). Such measurements, implemented, for example, with Faraday rotation on a detuned probe field [188], can create spin-squeezed states [189] and have been used to improve the sensitivity and bandwidth of atomic magnetometers [76,190] without adding additional noise. The bandwidth enhancement can be understood as a result of nondestructive spin-polarization measurements that can be made much more rapidly than the typical relaxation time of the atoms since the measured spin degree of freedom is unaffected by the measurement process. On time scales longer than the relaxation time (i.e., low frequencies), all quantum improvement typically disappears. Sensors utilizing spin squeezing were recently used for magnetic induction tomography [191]. The use of polarization-squeezed light reduces photon shot noise in the probe laser and has shown a similar improvement in both sensitivity [192,193] and bandwidth [194] of magnetometers. Superradiant lasers based on quantum-mechanically correlated atoms in an optical cavity have also been shown capable of precision magnetic field measurements [195]. Although entanglement has not been used for Rydberg atom sensors to the authors' knowledge yet, entanglement is used

in Rydberg atom neutral atom quantum computers and simulators [196]. When it comes to sensing with NV centers, one direction of current research (see [197] and references therein) is harnessing the normally detrimental dipole–dipole interactions among the color centers in dense ensembles to produce entangled collective spin states that can be used as a resource for sensing. Practical implementation of these advances will, undoubtedly, be the subject of future work.

5. FUTURE OUTLOOK

Atom-based quantum sensors are poised to bring dramatic new capability to a host of application spaces in the coming years. The unique capabilities embodied by these sensor modalities, including good long-term stability and accuracy, high spatial resolution, and inherent demodulation of carrier frequencies, are likely to enable new possibilities for the detection of electromagnetic fields. Features like the transparency and broad carrier bandwidth of Rydberg sensors are examples where a quantum sensor can be distinguished from its classical competition that do not involve sensitivity.

There is currently significant activity focused on the use of integrated photonics and micro-electrical-mechanical systems (MEMS) to achieve higher levels of integration, reduced size, and increased manufacturability for quantum sensors. Photonically integrated wavelength references [198,199], magnetometers [200], cavity quantum electrodynamics (cavity QED) systems [201,202], and cold atom systems [203,204] are all under development. For Rydberg atom sensors, photonic integrated circuits can make fast and dynamic tuning of the target RF frequency possible in a compact package, even enabling sensing at multiple frequencies achievable using the same coupling laser system [167]. Electro-optic combs to readout at multiple probe laser frequencies have also been demonstrated [205].

New methods are being developed to machine materials for microfabricated vapor cells including the use of femtosecond laser machining [206] and water-jet machining [207] that lower fabrication cost and allow a greater variety of materials and physical geometries to be used. New wafer-level fabrication approaches [208–210] are likely to reduce the cost of filling cells with alkali atoms, and new atomic species, such as alkaline earth atoms [211], will allow access to narrower optical transitions. For Rydberg atom sensing vapor cells, it is important to consider their engineering for properties like RF transparency [164]. The wavelength of RF waves offers the interesting possibility of engineering the interaction of the RF wave and the vapor cell [172,212]. These advances are driving atom-based sensors that rely on vapor cells closer to commercial viability, since the cost is decreasing along with increasing functionality and manufacturability.

Pulsed approaches to magnetometer operation [73–75,213–216] are likely to continue to make an impact in suppressing light shifts, improving long-term stability and heading errors, and reducing dead zones. New approaches to magnetic field gradiometry [213,217–222] will enable improved suppression of background field variations and allow more sensitive detection of localized sources such as magnetic anomalies or biomagnetic signals.

A major challenge in implementing squeezing and entanglement-based improvements to sensor performance is in maintaining the high fidelity of quantum correlations in metrologically meaningful settings where experimental imperfections are always present. Converting high degrees of entanglement and squeezing into correspondingly high improvements in instrument performance will be a major challenge for this field in the coming years. Rydberg sensors might benefit from squeezing since they are frequently limited by photon shot noise, and it is not possible to keep increasing the density of the Rydberg atoms. For real applications, the intensity of squeezed light sources and their size, weight, power consumption, and cost (SWaP-C) must be reduced. For many applications, the SWaP-C is far more important than the sensitivity increases offered by squeezing and entanglement.

Progress in improvement of NV-based sensor is closely related to the development of diamond materials and the ability to harness relaxation in dense ensembles of color centers. Among the multitude of future applications one can envision, for example, diagnostics at a level of a single biological cell and real-time guidance for microsurgery. A possible practical application of NV diamond sensing beyond magnetometry is rotation sensing (see [223] and references therein). Although currently not competitive with, for instance, atomic vapor-based nuclear magnetic resonance gyros, these systems may in the future replace all-solid-state sensors used in microchips and also be part of diamond *multisensors* potentially measuring magnetic field, rotations, and temperature at the same time.

Rydberg sensors can be anticipated to make their way into test and measurement applications soon. Future applications will hinge on features that separate them from antennas. Agile, broad bandwidth passive sensors for radar, spectrum sensing, and test and measurement appear to be on the horizon. Nevertheless, it should be pointed out that Rydberg atom sensors are complex. At least two lasers are used for the sensor. Both lasers have to have narrow spectral bandwidths, <1 MHz, and be externally stabilized. The coupling laser has to tune over several nm of spectral bandwidth to take advantage of the wide potential RF carrier bandwidth. Reading out the sensor at multiple RF frequencies around a Rydberg state requires tuning one of the lasers or the implementation of a frequency comb. Rapidly tuning the coupling laser using a low SWaP-C system is challenging [167]. The information about the RF wave is imprinted in the optical spectra and has to be translated into field amplitude (or power), phase, and polarization. Integrating and taking account of all these features in a single system, suitable for commercialization, is daunting, despite the fact that the technologies to meet the requirements largely exist. Integration of advanced technologies for Rydberg atom sensing will be critical for their implementation and a central theme going forward, perhaps more importantly than any fundamental research to explore their operation. Fundamentally, it is anticipated that it will be important to make Rydberg atom sensors more sensitive. It may be possible to make them more sensitive than an antenna-based RF receiver, but it has not been shown experimentally [140]. Likewise, facile phase detection that is performed at the maximum bandwidth of the Rydberg sensor is also an area of development. Broadband, all-optical phase readout is an increasing area of interest [224–228]. The engineering of vapor cells and the ability to overcome electric fields that interact with atoms is another challenge to be overcome.

6. CONCLUSION

In this paper, we briefly reviewed several representative types of quantum sensors based on atoms or atom-like systems (color centers in diamond). These technologies have been rapidly developing

over the past decade, and some of them (atomic vapor based magnetometers and NV diamond sensors) have already entered into the commercialization stage. This, in turn, has a positive feedback effect, catalyzing proliferation of applications and further improvement of the sensor technology. We have grounds to believe that this field will continue to show remarkable progress for years and decades ahead.

Funding. HORIZON EUROPE Framework Programme (HEU-RIA-MUQUABIS-101070546); Deutsche Forschungsgemeinschaft (DFG) (FKZ: SFB 1552/1 465145163); Bundesministerium für Bildung und Forschung (BMBF) (13N16455); Defense Advanced Research Projects Agency (HR00112190080); National Research Council Canada (QSP-058-1, QSP-105-1); National Institute of Standards and Technology (NIST on a Chip Program).

Acknowledgment. The authors thank James K. Thompson, Morgan W. Mitchell, Victor M. Acosta, Nir Bar-Gill, Fedor Jelezko, Fazhan Shi, and Pauli Kehayias for helpful discussions. The authors thank Ying-Ju Wang and Adam Biacchi for careful reading of the paper. Dmitry Budker was supported in part by the EU, DFG, and BMBF. James P. Shaffer thanks FedDev, Ontario, Defense Advanced Research Projects Agency (DARPA), and The National Research Council Internet of Things: Quantum Sensors Challenge program for support. John Kitching was supported by National Institute of Standards and Technology.

Disclosures. JPS, WaveRyde Instruments (IEPS)

Data availability. Data underlying the results presented in this paper are not publicly available at this time but may be obtained from the authors upon reasonable request.

REFERENCES

1. Y. Zhao, J. H. Zhang, J. H. Li, *et al.*, "A brief review of magnetic anomaly detection," Meas. Sci. Technol. **32**, 042002 (2021).
2. A. Sheinker, L. Frumkis, B. Ginzburg, *et al.*, "Magnetic anomaly detection using a three-axis magnetometer," IEEE Trans. Magn. **45**, 160–167 (2009).
3. M. D. Prouty, R. Johnson, I. Hrvoic, *et al.*, "Geophysical applications," in *Optical Magnetometry*, D. Budker and D. F. J. Kimball, eds. (Cambridge University, 2013), p. 319.
4. T. M. Tierney, N. Holmes, S. Mellor, *et al.*, "Optically pumped magnetometers: from quantum origins to multi-channel magnetoencephalography," NeuroImage **199**, 598–608 (2019).
5. M. J. Brookes, J. Leggett, M. Rea, *et al.*, "Magnetoencephalography with optically pumped magnetometers (OPM-MEG): the next generation of functional neuroimaging," Trends Neurosci. **45**, 621–634 (2022).
6. N. Aslam, H. Zhou, E. K. Urbach, *et al.*, "Quantum sensors for biomedical applications," Nat. Rev. Phys. **5**, 157–169 (2023).
7. M. Jiang, J. Bian, Q. Li, *et al.*, "Zero- to ultralow-field nuclear magnetic resonance and its applications," Fundam. Res. **1**, 68–84 (2021).
8. D. A. Barskiy, J. W. Blanchard, D. Budker, *et al.*, "Zero- to ultralow-field nuclear magnetic resonance," Prog. Nucl. Magn. Reson. Spectrosc. **148-149**, 101558 (2025).
9. C. Deans, T. Valenzuela, and M. Bason, "Quantum magnetometry for space," Proc. SPIE **12777**, 127776W (2023).
10. J. R. Maze, P. L. Stanwix, J. S. Hodges, *et al.*, "Nanoscale magnetic sensing with an individual electronic spin in diamond," Nature **455**, 644–647 (2008).
11. L. M. Pham, D. L. Sage, P. L. Stanwix, *et al.*, "Magnetic field imaging with nitrogen-vacancy ensembles," New J. Phys. **13**, 045021 (2011).
12. M. Garsi, R. Stöhr, A. Denisenko, *et al.*, "Three-dimensional imaging of integrated-circuit activity using quantum defects in diamond," Phys. Rev. Appl. **21**, 014055 (2024).
13. D. Le Sage, K. Arai, D. R. Glenn, *et al.*, "Optical magnetic imaging of living cells," Nature **496**, 486–489 (2013).
14. J. F. Barry, M. J. Turner, J. M. Schloss, *et al.*, "Optical magnetic detection of single-neuron action potentials using quantum defects in diamond," Proc. Natl. Acad. Sci. USA **113**, 14133 (2016).
15. T. S. Ghiasi, M. Borst, S. Kurdi, *et al.*, "Nitrogen-vacancy magnetometry of CRSBR by diamond membrane transfer," New J. Phys. **7**, 62 (2023).
16. R. Budakian, A. Finkler, A. Eichler, *et al.*, "Roadmap on nanoscale magnetic resonance imaging," Nanotechnology **35**, 412001 (2024).
17. R. Sobot, *Wireless Communication Electronics: Introduction to RF Circuits and Design Techniques* (Springer Cham, 2021).
18. L. Han and K. Wu, "Joint wireless communication and radar sensing systems–state of the art and future prospects," IET Microw. Antennas Propag. **7**, 876–885 (2013).
19. A. Manickavasagan and H. Jayasuriya, *Imaging with Electromagnetic Spectrum: Applications in Food and Agriculture* (Springer Berlin, 2014).
20. J. Stark, "Observations on the effect of the electrical field on spectral lines I transverse effect," Ann. Phys. Lpz. **43**, 965–982 (1914).
21. A. A. Clerk, M. H. Devoret, S. M. Girvin, *et al.*, "Introduction to quantum noise, measurement, and amplification," Rev. Mod. Phys. **82**, 1155 (2010).
22. L. Allen and J. H. Eberly, *Optical Resonance and Two-Level Atoms* (Dover, 1975).
23. F. Bloch, "Nuclear induction," Phys. Rev. **70**, 460 (1946).
24. W. Happer, "Optical pumping," Rev. Mod. Phys. **44**, 169 (1972).
25. E. Arimondo, "Coherent population trapping in laser spectroscopy," Prog. Opt. **35**, 257–354 (1996).
26. J. A. Sedlacek, A. Schwettmann, H. Kübler, *et al.*, "Atom-based vector microwave electrometry using rubidium Rydberg atoms in a vapor cell," Phys. Rev. Lett. **111**, 063001 (2013).
27. R. H. Dicke, "The effect of collisions upon the Doppler width of spectral lines," Phys. Rev. **89**, 472 (1953).
28. T. W. Hansch and A. L. Schawlow, "Cooling of gases by laser radiation," Opt. Commun. **13**, 68–69 (1975).
29. D. J. Wineland and H. Dehmelt, "Proposed $1014\Delta\nu < \nu$ laser fluorescence spectroscopy on Tl + mono-ion oscillator," Bull. Am. Phys. Soc. **20**, 637 (1975).
30. E. L. Hahn, "Spin echoes," Phys. Rev. **80**, 580 (1950).
31. W. Hanle, "Über magnetische beeinflussung der polarisation der resonanzfluoreszenz," Z. Phys. **30**, 93 (1924).
32. H. G. Dehmelt, "Modulation of a light beam by precessing absorbing atoms," Phys. Rev. **105**, 1924 (1957).
33. W. E. Bell and A. L. Bloom, "Optical detection of magnetic resonance in alkali metal vapor," Phys. Rev. **107**, 1559 (1957).
34. E. C. Beaty, P. L. Bender, and A. R. Chi, "Narrow hyperfine absorption lines of Cs^{133} in various buffer gases," Phys. Rev. **112**, 450 (1958).
35. W. E. Bell and A. L. Bloom, "Optically detected field-independent transition in sodium vapor," Phys. Rev. **109**, 219 (1958).
36. P. L. Bender, E. C. Beaty, and A. R. Chi, "Optical detection of narrow Rb^{87} hyperfine absorption lines," Phys. Rev. Lett. **1**, 311 (1958).
37. T. L. Skillman and P. L. Bender, "Measurement of the Earth's magnetic field with a rubidium vapor magnetometer," J. Geophys. Res. **63**, 513–515 (1958).
38. A. L. Bloom, "Principles of operation of the rubidium vapor magnetometer," Appl. Opt. **1**, 61–68 (1962).
39. N. F. Ness, T. L. Skillman, J. P. Heppner, *et al.*, "Measurements by a rocket-borne rubidium vapor magnetometer," J. Geophys. Res. **66**, 2549 (1961).
40. D. Budker and D. F. J. Kimball, *Optical Magnetometry* (Cambridge University, 2013).
41. J. Kitching, S. Knappe, and E. A. Donley, "Atomic sensors-a review," IEEE Sens. J. **11**, 1749–1758 (2011).
42. D. Budker and M. Romalis, "Optical magnetometry," Nat. Phys. **3**, 227–234 (2007).
43. A. Fabricant, I. Novikova, and G. Bison, "How to build a magnetometer with thermal atomic vapor: a tutorial," New J. Phys. **25**, 025001 (2023).
44. E. B. Alexandrov and A. K. Vershovskiy, "Mx and Mz magnetometers," in *Optical Magnetometry*, D. Budker and D. F. J. Kimball, eds. (Cambridge University, 2013), p. 60.
45. D. C. Hovde, M. D. Prouty, I. Hrvoic, *et al.*, "Commercial magnetometers and their applications," in *Optical Magnetometry*, D. Budker and D. F. J. Kimball, eds. (Cambridge University, 2013), p. 387.
46. D. F. J. Kimball, S. Pustelny, V. V. Yaschuk, *et al.*, "Optical magnetometry with modulated light," in *Optical Magnetometry*, D. Budker and D. F. J. Kimball, eds. (Cambridge University, 2013), p. 104.
47. W. E. Bell and A. L. Bloom, "Optically driven spin precession," Phys. Rev. Lett. **6**, 280 (1961).

48. M. O. Scully and M. Fleischhauer, "High-sensitivity magnetometer based on index-enhanced media," Phys. Rev. Lett. **69**, 1360–1363 (1992).
49. A. Nagel, L. Graf, A. Naumov, *et al.*, "Experimental realization of coherent dark-state magnetometers," Europhys. Lett. **44**, 31 (1998).
50. R. Lammegger, A. Huss, L. Windholz, *et al.*, "All optical magnetometer based on electromagnetically induced transparency," Proc. SPIE **5532**, 380 (2004).
51. J. Belfi, G. Bevilacqua, V. Biancalana, *et al.*, "All optical sensor for automated magnetometry based on coherent population trapping," J. Opt. Soc. Am. B **24**, 1482–1489 (2007).
52. J. M. Higbie, S. M. Rochester, B. Patton, *et al.*, "Magnetometry with mesospheric sodium," Proc. Natl. Acad. Sci. USA **108**, 3522–3525 (2011).
53. B. Patton, O. O. Versolato, D. C. Hovde, *et al.*, "A remotely interrogated all-optical Rb-87 magnetometer," Appl. Phys. Lett. **101**, 083502 (2012).
54. K. Levi, A. Giat, L. Golan, *et al.*, "Remote chip-scale quantum sensing of magnetic fields," arXiv (2023).
55. A. M. Akulshin, D. Budker, F. Pedreros Bustos, *et al.*, "Remote detection optical magnetometry," Phys. Rep. **1106**, 1–32 (2025).
56. A. Pollinger, R. Lammegger, W. Magnes, *et al.*, "Coupled dark state magnetometer for the China Seismo-Electromagnetic Satellite," Meas. Sci. Technol. **29**, 095103 (2018).
57. B. Zhou, B. J. Cheng, X. C. Gou, *et al.*, "First in-orbit results of the vector magnetic field measurement of the high precision magnetometer onboard the China Seismo-Electromagnetic Satellite," Earth Planets Space **71**, 119 (2019).
58. A. R. Keyser, J. A. Rice, and L. D. Schearer, "Metastable helium magnetometer for observing small geomagnetic fluctuations," J. Geophys. Res. **66**, 4163–4169 (1961).
59. R. E. Slocum and F. N. Reilly, "Low field helium magnetometer for space applications," IEEE Trans. Nucl. Sci. **10**, 165–171 (1963).
60. R. E. Slocum, D. D. McGregor, and A. W. Brown, "Helium magnetometers," in *Optical Magnetometry*, D. Budker and D. F. J. Kimball, eds. (Cambridge University, 2013), p. 190.
61. R. E. Slocum, "Advances in laser-pumped helium magnetometers for space applications," Rev. Sci. Instrum. **61**, 2984 (1990).
62. S. Kellock, P. Auston, A. Balogh, *et al.*, "Cassini dual technique magnetometer instrument," Proc. SPIE **2803**, 141 (1996).
63. T. G. Walker and W. Happer, "Spin-exchange optical pumping of noble-gas nuclei," Rev. Mod. Phys. **69**, 629 (1997).
64. C. Gemmel, W. Heil, S. Karpuk, *et al.*, "Ultra-sensitive magnetometry based on free precession of nuclear spins," Eur. Phys. J. D **57**, 303–320 (2010).
65. W. Happer and B. S. Mathur, "Effective operator formalism in optical pumping," Phys. Rev. **163**, 12 (1967).
66. B. R. Bulos, A. Marshall, and W. Happer, "Light shifts due to real transitions in optically pumped alkali atoms," Phys. Rev. A **4**, 51 (1971).
67. A. A. Podvyaznyi, A. A. Sakantsev, and V. V. Semenov, "About the Zeeman light-induced frequency shift of the radio-optical resonance in optically oriented isotopes of alkali metals," Russ. Phys. J. **46**, 933–935 (2003).
68. M. Fleischhauer, A. B. Matsko, and M. O. Scully, "Quantum limit of optical magnetometry in the presence of AC stark shifts," Phys. Rev. A **62**, 013808 (2000).
69. I. Novikova, A. B. Matsko, V. L. Velichansky, *et al.*, "Compensation of AC stark shifts in optical magnetometry," Phys. Rev. A **63**, 063802 (2001).
70. V. I. Yudin, A. V. Taichenachev, Y. O. Dudin, *et al.*, "Vector magnetometry based on electromagnetically induced transparency in linearly polarized light," Phys. Rev. A **82**, 033807 (2010).
71. I. A. Sulai, R. Wyllie, M. Kauer, *et al.*, "Diffusive suppression of AC-stark shifts in atomic magnetometers," Opt. Lett. **38**, 974–976 (2013).
72. E. Zhivun, A. Wickenbrock, J. Sudyka, *et al.*, "Vector light shift averaging in paraffin-coated alkali vapor cells," Opt. Express **24**, 15383–15390 (2016).
73. G. Vasilakis, V. Shah, and M. V. Romalis, "Stroboscopic backaction evasion in a dense alkali-metal vapor," Phys. Rev. Lett. **106**, 143601 (2011).
74. D. Sheng, S. Li, N. Dural, *et al.*, "Subfemtotesla scalar atomic magnetometry using multipass cells," Phys. Rev. Lett. **110**, 160802 (2013).
75. M. E. Limes, E. L. Foley, T. W. Kornack, *et al.*, "Portable magnetometry for detection of biomagnetism in ambient environments," Phys. Rev. Appl. **14**, 011002 (2020).
76. V. Shah, G. Vasilakis, and M. V. Romalis, "High bandwidth atomic magnetometery with continuous quantum nondemolition measurements," Phys. Rev. Lett. **104**, 013601 (2010).
77. G. Bao, D. Kanta, D. Antypas, *et al.*, "All-optical spin locking in alkali-metal-vapor magnetometers," Phys. Rev. A **105**, 043109 (2022).
78. E. Zhivun, A. Wickenbrock, B. Patton, *et al.*, "Alkali-vapor magnetic resonance driven by fictitious radiofrequency fields," Appl. Phys. Lett. **105**, 192406 (2014).
79. B. Patton, E. Zhivun, D. Hovde, *et al.*, "All-optical vector atomic magnetometer," Phys. Rev. Lett. **113**, 013001 (2014).
80. H. G. Dehmelt, "Slow spin relaxation of optically polarized sodium atoms," Phys. Rev. **105**, 1487 (1957).
81. W. Franzen, "Spin relaxation of optically aligned rubidium vapor," Phys. Rev. **115**, 850 (1959).
82. W. Happer and H. Tang, "Spin-exchange shift and narrowing of magnetic resonance lines in optically pumped alkali vapors," Phys. Rev. Lett. **31**, 273 (1973).
83. W. Happer and A. C. Tam, "Effect of rapid spin exchange on magnetic-resonance spectrum of alkali vapors," Phys. Rev. A **16**, 1877 (1977).
84. I. Savukov and S. J. Seltzer, "Spin-exchange-relaxation-free (SERF) magnetometers," in *Optical Magnetometry*, D. Budker and D. F. J. Kimball, eds. (Cambridge University, 2013), p. 85.
85. I. K. Kominis, T. W. Kornack, J. C. Allred, *et al.*, "A subfemtotesla multichannel atomic magnetometer," Nature **422**, 596–599 (2003).
86. J. C. Allred, R. N. Lyman, T. W. Kornack, *et al.*, "High-sensitivity atomic magnetometer unaffected by spin-exchange relaxation," Phys. Rev. Lett. **89**, 130801 (2002).
87. H. B. Dang, A. C. Maloof, and M. V. Romalis, "Ultrahigh sensitivity magnetic field and magnetization measurements with an atomic magnetometer," Appl. Phys. Lett. **97**, 151110 (2010).
88. P. D. D. Schwindt, S. Knappe, V. Shah, *et al.*, "Chip-scale atomic magnetometer," Appl. Phys. Lett. **85**, 6409–6411 (2004).
89. P. D. D. Schwindt, B. Lindseth, S. Knappe, *et al.*, "A chip-scale atomic magnetometer with improved sensitivity using the Mx technique," Appl. Phys. Lett. **90**, 081102 (2007).
90. L. A. Liew, S. Knappe, J. Moreland, *et al.*, "Microfabricated alkali atom vapor cells," Appl. Phys. Lett. **84**, 2694–2696 (2004).
91. S. Knappe, P. D. D. Schwindt, V. Shah, *et al.*, "A chip-scale atomic clock based on ^{87}Rb with improved frequency stability," Opt. Express **13**, 1249–1253 (2005).
92. H. Raghavan, M. C. D. Tayler, K. Mouloudakis, *et al.*, "Functionalized millimeter-scale vapor cells for alkali-metal spectroscopy and magnetometry," Phys. Rev. Appl. **22**, 044011 (2024).
93. V. Gerginov, S. Krzyzewski, and S. Knappe, "Pulsed operation of a miniature scalar optically pumped magnetometer," J. Opt. Soc. Am. B **34**, 1429–1434 (2017).
94. V. Shah, S. Knappe, P. D. D. Schwindt, *et al.*, "Subpicotesla atomic magnetometry with a microfabricated vapour cell," Nat. Photonics **1**, 649–652 (2007).
95. B. J. Anderson, M. H. Acuna, D. A. Lohr, *et al.*, "The magnetometer instrument on messenger," Space Sci. Rev. **131**, 417–450 (2007).
96. H. C. Séran and P. Fergeau, "An optimized low-frequency three-axis search coil magnetometer for space research," Rev. Sci. Instrum. **76**, 044502 (2005).
97. I. Mateos, B. Patton, E. Zhivun, *et al.*, "Noise characterization of an atomic magnetometer at sub-millihertz frequencies," Sens. Actuators A **224**, 147–155 (2015).
98. F. Bertrand, T. Jager, A. Boness, *et al.*, "A ^{4}He vector zero-field optically pumped magnetometer operated in the Earth-field," Rev. Sci. Instrum. **92**, 105005 (2021).
99. N. Wilson, P. Light, A. Luiten, *et al.*, "Ultrastable optical magnetometry," Phys. Rev. Appl. **11**, 044034 (2019).
100. S. Groeger, G. Bison, and A. Weis, "Design and performance of laser-pumped Cs-magnetometers for the planned UCN EDM experiment at PSI," J. Res. Natl. Inst. Stand. Technol. **110**, 179–183 (2005).
101. J. H. Storm, P. Hommen, D. Drung, *et al.*, "An ultra-sensitive and wideband magnetometer based on a superconducting quantum interference device," Appl. Phys. Lett. **110**, 072603 (2017).
102. W. C. Griffith, S. Knappe, and J. Kitching, "Femtotesla atomic magnetometry in a microfabricated vapor cell," Opt. Express **18**, 27167–27172 (2010).

103. A. Nikiel, P. Blümler, W. Heil, *et al.*, "Ultrasensitive ^{3}He magnetometer for measurements of high magnetic fields," Eur. Phys. J. D **68**, 330 (2014).
104. E. Boto, N. Holmes, J. Leggett, *et al.*, "Moving magnetoencephalography towards real-world applications with a wearable system," Nature **555**, 657–661 (2018).
105. W. Gawlik and J. Higbie, "Magnetometery with cold atoms and BEC," in *Optical Magnetometry*, D. Budker and D. F. Jackson Kimball, eds. (Cambridge University, 2013), p. 167.
106. D. F. Jackson Kimball, D. Budker, T. E. Chupp, *et al.*, "Probing fundamental physics with spin-based quantum sensors," Phys. Rev. A **108**, 010101 (2023).
107. S. Wildermuth, S. Hofferberth, I. Lesanovsky, *et al.*, "Bose-Einstein condensates-microscopic magnetic-field imaging," Nature **435**, 440 (2005).
108. S. Wildermuth, S. Hofferberth, I. Lesanovsky, *et al.*, "Sensing electric and magnetic fields with Bose-Einstein condensates," Appl. Phys. Lett. **88**, 264103 (2006).
109. F. Yang, A. J. Kollár, S. F. Taylor, *et al.*, "Scanning quantum cryogenic atom microscope," Phys. Rev. Appl. **7**, 034026 (2017).
110. B. Dellabetta, T. L. Hughes, M. J. Gilbert, *et al.*, "Imaging topologically protected transport with quantum degenerate gases," Phys. Rev. B **85**, 205442 (2012).
111. D. C. Aveline, J. R. Williams, E. R. Elliott, *et al.*, "Observation of Bose-Einstein condensates in an Earth-orbiting research lab," Nature **582**, 193–197 (2020).
112. A. Canciani and J. Raquet, "Airborne magnetic anomaly navigation," IEEE Trans. Aerosp. Electron. Syst. **53**, 67–80 (2017).
113. G. Bison, R. Wynands, and A. Weis, "Dynamical mapping of the human cardiomagnetic field with a room-temperature, laser-optical sensor," Opt. Express **11**, 904–909 (2003).
114. H. Xia, A. B. A. Baranga, D. Hoffman, *et al.*, "Magnetoencephalography with an atomic magnetometer," Appl. Phys. Lett. **89**, 211104 (2006).
115. J. S. Bennett, B. E. Vyhnalek, H. Greenall, *et al.*, "Precision magnetometers for aerospace applications: a review," Sensors **21**, 5568 (2021).
116. D. F. Jackson Kimball, S. K. Lamoreaux, and T. E. Chupp, "Tests of fundamental physics with optical magnetometers," in *Optical Magnetometry*, D. Budker and D. F. J. Kimball, eds. (Cambridge University, 2013), p. 339.
117. B. J. Cheng, B. Zhou, W. Magnes, *et al.*, "Performance of the engineering model of the CSES high precision magnetometer," in *IEEE Sensors Conference* (2015), p. 1933.
118. W. Gawlik and S. Pustelny, "Nonlinear magneto-optical rotation magnetometers," in *High Sensitivity Magnetometers*, A. Grosz, M. J. Haji-Sheikh, and S. C. Mukhopadhyay, eds. (Springer International Publishing, 2017), p. 425.
119. V. Gerginov, M. Pomponio, and S. Knappe, "Scalar magnetometry below 100 fT/Hz$^{1/2}$ in a microfabricated cell," IEEE Sens. J. **20**, 12684 (2020).
120. R. Zhang, D. Kanta, A. Wickenbrock, *et al.*, "Heading-error-free optical atomic magnetometry in the Earth-field range," Phys. Rev. Lett. **130**, 153601 (2023).
121. J. Taylor, P. Cappellaro, L. Childress, *et al.*, "High-sensitivity diamond magnetometer with nanoscale resolution," Nat. Phys. **4**, 810–816 (2008).
122. J. Zhang and D. Suter, "Single NV centers as sensors for radio-frequency fields," Phys. Rev. Res. **5**, L022026 (2023).
123. M. W. Doherty, N. B. Manson, P. Delaney, *et al.*, "The nitrogen-vacancy colour centre in diamond," Phys. Rep. **528**, 1–45 (2013).
124. A. T. Younesi, M. Omar, A. Wickenbrock, *et al.*, "Towards high-sensitivity magnetometry with nitrogen vacancy centers in diamond using the singlet infrared absorption," arXiv (2024).
125. K. Jensen, P. Kehayias, and D. Budker, "Magnetometry with nitrogen-vacancy centers in diamond," in *High Sensitivity Magnetometers* (Springer, 2017), pp. 553–576.
126. J. F. Barry, J. M. Schloss, E. Bauch, *et al.*, "Sensitivity optimization for NV-diamond magnetometry," Rev. Mod. Phys. **92**, 015004 (2020).
127. E. Marchiori, L. Ceccarelli, N. Rossi, *et al.*, "Nanoscale magnetic field imaging for 2D materials," Nat. Rev. Phys. **4**, 49–60 (2022).
128. E. Herbschleb, H. Kato, Y. Maruyama, *et al.*, "Ultra-long coherence times amongst room-temperature solid-state spins," Nat. Commun. **10**, 3766 (2019).
129. Z. Zhao, X. Ye, S. Xu, *et al.*, "Sub-nanotesla sensitivity at the nanoscale with a single spin," Natl. Sci. Rev. **10**, nwad100 (2023).
130. I. Fescenko, A. Jarmola, I. Savukov, *et al.*, "Diamond magnetometer enhanced by ferrite flux concentrators," Phys. Rev. Res. **2**, 023394 (2020).
131. J. F. Barry, M. H. Steinecker, S. T. Alsid, *et al.*, "Sensitive AC and DC magnetometry with nitrogen-vacancy-center ensembles in diamond," Phys. Rev. Appl. **22**, 044069 (2024).
132. Y. Xie, H. Yu, Y. Zhu, *et al.*, "A hybrid magnetometer towards femtotesla sensitivity under ambient conditions," Sci. Bull. **66**(2), 127–132 (2021).
133. Y. Silani, J. Smits, I. Fescenko, *et al.*, "Nuclear quadrupole resonance spectroscopy with a femtotesla diamond magnetometer," Sci. Adv. **9**, eadh3189 (2023).
134. S. T. Alsid, J. M. Schloss, M. H. Steinecker, *et al.*, "Solid-state microwave magnetometer with picotesla-level sensitivity," Phys. Rev. Appl. **19**, 054095 (2023).
135. C. L. Degen, F. Reinhard, and P. Cappellaro, "Quantum sensing," Rev. Mod. Phys. **89**, 035002 (2017).
136. D. Farfurnik, A. Jarmola, D. Budker, *et al.*, "Spin ensemble-based ac magnetometry using concatenated dynamical decoupling at low temperatures," J. Opt. **20**, 024008 (2018).
137. V. M. Acosta, L. S. Bouchard, D. Budker, *et al.*, "Color centers in diamond as novel probes of superconductivity," J. Supercond. Novel Magn. **32**, 85–95 (2019).
138. K. Arai, A. Kuwahata, D. Nishitani, *et al.*, "Millimetre-scale magnetocardiography of living rats with thoracotomy," Commun. Phys. **5**, 200 (2022).
139. Y. Ninio, N. Waiskopf, I. Meirzada, *et al.*, "High-sensitivity, high-resolution detection of reactive oxygen species concentration using NV centers," ACS Photonics **8**, 1917–1921 (2021).
140. H. Fan, S. Kumar, J. Sedlacek, *et al.*, "Atom based RF electric field sensing," J. Phys. B **48**, 202001 (2015).
141. C. S. Adams, J. D. Pritchard, and J. P. Shaffer, "Rydberg atom quantum technologies," J. Phys. B **53**, 012002 (2020).
142. D. H. Meyer, Z. A. Castillo, K. C. Cox, *et al.*, "Assessment of Rydberg atoms for wideband electric field sensing," J. Phys. B **53**, 034001 (2020).
143. C. T. Fancher, D. R. Scherer, M. C. S. John, *et al.*, "Rydberg atom electric field sensors for communications and sensing," IEEE Trans. Quantum Eng. **2**, 3501313 (2021).
144. M. Simons, A. Artusio-Glimpse, A. Robinson, *et al.*, "Rydberg atom-based sensors for radio-frequency electric field metrology, sensing, and communications," *The Proceedings of the IMEKO World Congress*, Yokohama, Japan, 2021, p. 18.
145. H. Zhang, Y. Ma, K. Liao, *et al.*, "Rydberg atom electric field sensing for metrology, communication and hybrid quantum systems," Sci. Bull. **69**(10), 1515–1535 (2024).
146. S. Borówka, U. Pylypenko, M. Mazelanik, *et al.*, "Continuous wideband microwave-to-optical converter based on room-temperature Rydberg atoms," Nat. Photonics **18**, 32 (2024).
147. C. Holloway, M. Simons, A. Haddab, *et al.*, "A Rydberg atom-based mixer: measuring the phase of a radio frequency wave," Appl. Phys. Lett. **114**, 114101 (2019).
148. M. Jing, Y. Hu, J. Ma, *et al.*, "Atomic superheterodyne receiver based on microwave-dressed Rydberg spectroscopy," Nat. Phys. **16**, 911–915 (2020).
149. N. Prajapati, N. Bhusal, A. P. Rotunno, *et al.*, "Sensitivity comparison of two-photon vs three-photon Rydberg electrometry," J. Appl. Phys. **134**, 023101 (2023).
150. J. A. Sedlacek, A. Schwettmann, H. Kübler, *et al.*, "Microwave electrometry with Rydberg atoms in a vapour cell using bright atomic resonances," Nat. Phys. **8**, 819–824 (2012).
151. J. P. Shaffer and H. Kübler, "A read-out enhancement for microwave electric field sensing with Rydberg atoms," Proc. SPIE **10674**, 106740C (2018).
152. S. M. Bohaichuk, F. Ripka, V. Venu, *et al.*, "Three-photon Rydberg-atom-based radio-frequency sensing scheme with narrow linewidth," Phys. Rev. Appl. **20**, L061004 (2023).
153. N. Thaicharoen, K. R. Moore, D. A. Anderson, *et al.*, "Electromagnetically induced transparency, absorption, and microwave-field sensing in a Rb vapor cell with a three-color all-infrared laser system," Phys. Rev. A **100**, 063427 (2019).
154. N. Prajapati, S. Berweger, A. P. Rotunno, *et al.*, "Investigation of fluorescence versus transmission readout for three-photon Rydberg excitation used in electrometry," AVS Quantum Sci. **6**, 034401 (2024).

155. M. Fleischhauer, A. Imamoglu, and J. P. Marangos, "Electromagnetically induced transparency: optics in coherent media," Rev. Mod. Phys. **77**, 633–673 (2005).
156. M. T. Simons, M. D. Kautz, C. L. Holloway, *et al.*, "Electromagnetically induced transparency (EIT) and Autler-Townes (AT) splitting in the presence of band-limited white Gaussian noise," J. Appl. Phys. **123**, 203105 (2018).
157. E. B. Norrgard, S. P. Eckel, C. L. Holloway, *et al.*, "Quantum blackbody thermometry," New J. Phys. **23**, 033037 (2021).
158. M. Schmidt, S. Bohaichuk, V. Venu, *et al.*, "Rydberg-atom-based radio-frequency sensors: amplitude-regime sensing," Opt. Express **32**, 27768–27791 (2024).
159. M. V. Romalis, J. Wiedemann, S. Zhang, *et al.*, "Vapor cell Rydberg atom electrometry with time-separated fields," arXiv (2024).
160. 3GPP, "NR base station conformance testing, part 1: radiated conformance testing, release 16," Tech. Rep. TS 38.141-1, v16.3.0 (3GPP Technical Specification Group Radio Access Network, 2020).
161. 3GPP, "NR base station conformance testing, part 2: radiated conformance testing, release 16," Tech. Rep. TS 38.141-2, v16.3.0 (3GPP Technical Specification Group Radio Access Network, 2020).
162. H. Fan, S. Kumar, J. Sheng, *et al.*, "Effect of vapor-cell geometry on Rydberg-atom-based measurements of radio-frequency electric fields," Phys. Rev. Appl. **4**, 044015 (2015).
163. L. Zhang, J. Liu, Y. Jia, *et al.*, "Vapor cell geometry effect on Rydberg atom-based microwave electric field measurement," Chin. Phys. B **27**, 033201 (2018).
164. M. Noaman, H. Amarloo, R. Pandiyan, *et al.*, "Vapor cell characterization and optimization for applications in Rydberg atom-based radio frequency sensing," Proc. SPIE **12447**, 124470V (2023).
165. S. Liu, Z. Li, L. Zhang, *et al.*, "The realization of disturbance-reduction small vapor cells for broadband microwave detection with Rydberg atoms," IEEE Electron Device Lett. **45**, 1622–1625 (2024).
166. J. A. Gordon, C. L. Holloway, S. Jefferts, *et al.*, "Quantum-based Si traceable electric-field probe," in *IEEE International Symposium on Electromagnetic Compatibility* (2010), p. 321.
167. C. Liu, K. Nickerson, D. W. Booth, *et al.*, "Stable, narrow-linewidth laser system with a broad frequency tunability and a fast switching time," Opt. Lett. **49**, 399–402 (2024).
168. R. Gold, "Optimal binary sequences for spread spectrum multiplexing (corresp.)," IEEE Trans. Inf. Theory **13**, 619–621 (2006).
169. D. A. Anderson, E. G. Paradis, and G. Raithel, "A vapor-cell atomic sensor for radio-frequency field detection using a polarization-selective field enhancement resonator," Appl. Phys. Lett. **113**, 073501 (2018).
170. M. T. Simons, A. H. Haddab, and J. A. Gordon, "Waveguide-integrated Rydberg atom-based RF field detector for near-field antenna measurements," in *Antenna Measurement Techniques Association Symposium (AMTA)* (2019), pp. 1–4.
171. C. L. Holloway, N. Prajapati, A. B. Artusio-Glimpse, *et al.*, "Rydberg atom-based field sensing enhancement using a split-ring resonator," Appl. Phys. Lett. **120**, 204001 (2022).
172. H. Amarloo, M. Noaman, S.-P. Yu, *et al.*, "A photonic crystal receiver for Rydberg atom-based sensing," Commun. Eng. **4**, 70 (2024).
173. M. I. Skolnik, *Introduction to Radar Systems* (McGraw Hill, 2000).
174. H. Vahlbruch, M. Mehmet, K. Danzmann, *et al.*, "Detection of 15 dB squeezed states of light and their application for the absolute calibration of photoelectric quantum efficiency," Phys. Rev. Lett. **117**, 110801 (2016).
175. O. Hosten, N. J. Engelsen, R. Krishnakumar, *et al.*, "Measurement noise 100 times lower than the quantum-projection limit using entangled atoms," Nature **529**, 505–508 (2016).
176. K. C. Cox, G. P. Greve, J. M. Weiner, *et al.*, "Deterministic squeezed states with collective measurements and feedback," Phys. Rev. Lett. **116**, 093602 (2016).
177. J. Aasi, J. Abadie, B. P. Abbott, *et al.*, "Enhanced sensitivity of the LIGO gravitational wave detector by using squeezed states of light," Nat. Photonics **7**, 613–619 (2013).
178. Ligo-Detector-Collaboration, D. Ganapathy and W. Jia, "Broadband quantum enhancement of the LIGO detectors with frequency-dependent squeezing," Phys. Rev. X **13**, 041021 (2023).
179. B. Braverman, A. Kawasaki, E. Pedrozo-Penafiel, *et al.*, "Near-unitary spin squeezing in Yb-171," Phys. Rev. Lett. **122**, 223203 (2019).
180. E. Pedrozo-Penafiel, S. Colombo, C. Shu, *et al.*, "Entanglement on an optical atomic-clock transition," Nature **588**, 414–418 (2020).
181. G. P. Greve, C. Luo, B. Wu, *et al.*, "Entanglement-enhanced matter-wave interferometry in a high-finesse cavity," Nature **610**, 472–477 (2022).
182. C. Cassens, B. Meyer-Hoppe, E. Rasel, *et al.*, "An entanglement-enhanced atomic gravimeter," arXiv (2024).
183. J. M. Robinson, M. Miklos, Y. M. Tso, *et al.*, "Direct comparison of two spin-squeezed optical clock ensembles at the 10^{-17} level," Nat. Phys. **20**, 208–213 (2024).
184. S. F. Huelga, C. Macchiavello, T. Pellizzari, *et al.*, "Improvement of frequency standards with quantum entanglement," Phys. Rev. Lett. **79**, 3865 (1997).
185. M. Auzinsh, D. Budker, D. F. Kimball, *et al.*, "Can a quantum nondemolition measurement improve the sensitivity of an atomic magnetometer?" Phys. Rev. Lett. **93**, 173002 (2004).
186. E. M. Kessler, P. Komar, M. Bishof, *et al.*, "Heisenberg-limited atom clocks based on entangled qubits," Phys. Rev. Lett. **112**, 190403 (2014).
187. V. B. Braginsky, Y. I. Vorontsov, and K. S. Thorne, "Quantum nondemolition measurements," Science **209**, 547–557 (1980).
188. A. Kuzmich, N. P. Bigelow, and L. Mandel, "Atomic quantum nondemolition measurements and squeezing," Europhys. Lett. **42**, 481 (1998).
189. D. J. Wineland, J. J. Bollinger, W. M. Itano, *et al.*, "Spin squeezing and reduced quantum noise in spectroscopy," Phys. Rev. A **46**, R6797 (1992).
190. R. J. Sewell, M. Koschorreck, M. Napolitano, *et al.*, "Magnetic sensitivity beyond the projection noise limit by spin squeezing," Phys. Rev. Lett. **109**, 253605 (2012).
191. W. Q. Zheng, H. Y. Wang, R. Schmieg, *et al.*, "Entanglement-enhanced magnetic induction tomography," Phys. Rev. Lett. **130**, 203602 (2023).
192. F. Wolfgramm, A. Cere, F. A. Beduini, *et al.*, "Squeezed-light optical magnetometry," Phys. Rev. Lett. **105**, 053601 (2010).
193. T. Horrom, R. Singh, J. P. Dowling, *et al.*, "Quantum-enhanced magnetometer with low-frequency squeezing," Phys. Rev. A **86**, 023803 (2012).
194. C. Troullinou, R. Jiménez-Martínez, J. Kong, *et al.*, "Squeezed-light enhancement and backaction evasion in a high sensitivity optically pumped magnetometer," Phys. Rev. Lett. **127**, 193601 (2021).
195. J. M. Weiner, K. C. Cox, J. G. Bohnet, *et al.*, "Superradiant Raman laser magnetometer," Appl. Phys. Lett. **101**, 261107 (2012).
196. M. Saffman, T. J. Walker, and K. Molmer, "Quantum information with Rydberg atoms," Rev. Mod. Phys. **82**, 2313-2363 (2010).
197. H. Gao, L. S. Martin, L. B. Hughes, *et al.*, "Signal amplification in a solid-state quantum sensor via asymmetric time-reversal of many-body dynamics," Nature **646**, 68–73 (2025).
198. M. T. Hummon, S. Kang, D. G. Bopp, *et al.*, "Photonic chip for laser stabilization to an atomic vapor with 10^{-11} instability," Optica **5**, 443–449 (2018).
199. R. Zektzer, M. T. Hummon, L. Stern, *et al.*, "A chip-scale optical frequency reference for the telecommunication band based on acetylene," Laser Photonics Rev. **14**, 1900414 (2020).
200. Y. Sebbag, E. Talker, A. Naiman, *et al.*, "Demonstration of an integrated nanophotonic chip-scale alkali vapor magnetometer using inverse design," Light Sci. Appl. **10**, 54 (2021).
201. H. Alaeian, R. Ritter, M. Basic, *et al.*, "Cavity QED based on room temperature atoms interacting with a photonic crystal cavity: a feasibility study," Appl. Phys. B **126**, 25 (2020).
202. R. Zektzer, X. Lu, K. T. Hoang, *et al.*, "Strong interactions between integrated microresonators and alkali atomic vapors: towards single-atom, single-photon operation," Optica **11**, 1376–1384 (2024).
203. A. Isichenko, N. Chauhan, D. Bose, *et al.*, "Photonic integrated beam delivery for a rubidium 3D magneto-optical trap," Nat. Commun. **14**, 3080 (2023).
204. J. P. McGilligan, K. Gallacher, P. F. Griffin, *et al.*, "Micro-fabricated components for cold atom sensors," Rev. Sci. Instrum. **93**, 091101 (2022).
205. K. Dixon, K. Nickerson, D. W. Booth, *et al.*, "Rydberg-atom-based electrometry using a self-heterodyne frequency-comb readout and preparation scheme," Phys. Rev. Appl. **19**, 034078 (2023).
206. V. G. Lucivero, A. Zanoni, G. Corrielli, *et al.*, "Laser-written vapor cells for chip-scale atomic sensing and spectroscopy," Opt. Express **30**, 27149–27163 (2022).
207. S. Dyer, P. F. Griffin, A. S. Arnold, *et al.*, "Micro-machined deep silicon atomic vapor cells," J. Appl. Phys. **132**, 134401 (2022).

208. D. G. Bopp, V. M. Maurice, and J. E. Kitching, "Wafer-level fabrication of alkali vapor cells using in-situ atomic deposition," J. Phys. Photonics **3**, 015002 (2020).
209. Y. Li, D. B. Sohn, M. T. Hummon, *et al.*, "Wafer-scale fabrication of evacuated alkali vapor cells," Opt. Lett. **49**, 4963–4966 (2024).
210. V. Maurice, C. Carle, S. Keshavarzi, *et al.*, "Wafer-level vapor cells filled with laser-actuated hermetic seals for integrated atomic devices," Microsyst. Nanoeng. **8**, 129 (2022).
211. J. M. Pate, J. Kitching, and M. T. Hummon, "Microfabricated strontium atomic vapor cells," Opt. Lett. **48**, 383–386 (2023).
212. H. Amarloo, J. Ramirez-Serrano, and J. P. Shaffer, "Vapor cells having reduced scattering cross-sections and their methods of manufacture," U.S. patent 10,605,840 (2020).
213. V. G. Lucivero, W. Lee, N. Dural, *et al.*, "Femtotesla direct magnetic gradiometer using a single multipass cell," Phys. Rev. Appl. **15**, 014004 (2021).
214. M. E. Limes, L. Rathbun, E. Foley, *et al.*, "Frequency-dependent amplitude correction to free-precession scalar magnetometers," IEEE Sens. Lett. **9**, 1–4 (2025).
215. C. Kiehl, T. S. Menon, D. P. Hewatt, *et al.*, "Correcting heading errors in optically pumped magnetometers through microwave interrogation," Phys. Rev. Appl. **22**, 014005 (2024).
216. D. P. Hewatt, M. Ellmeier, C. Kiehl, *et al.*, "Investigating the hyperfine systematic error and relative phase in low-spin-polarization alkali-metal free-induction-decay magnetometers," Phys. Rev. A **111**, 033106 (2025).
217. D. Sheng, A. R. Perry, S. P. Krzyzewski, *et al.*, "A microfabricated optically-pumped magnetic gradiometer," Appl. Phys. Lett. **110**, 031106 (2017).
218. M. Jiang, R. P. Frutos, T. Wu, *et al.*, "Magnetic gradiometer for the detection of zero- to ultralow-field nuclear magnetic resonance," Phys. Rev. Appl. **11**, 024005 (2019).
219. A. R. Perry, M. D. Bulatowicz, M. Larsen, *et al.*, "All-optical intrinsic atomic gradiometer with sub-20 fT/cm/Hz$^{1/2}$ sensitivity in a 22 μT earth-scale magnetic field," Opt. Express **28**, 36696–36705 (2020).
220. K. Campbell, Y. J. Wang, I. Savukov, *et al.*, "Gradient field detection using interference of stimulated microwave optical sidebands," Phys. Rev. Lett. **128**, 163602 (2022).
221. V. G. Lucivero, W. Lee, T. W. Kornack, *et al.*, "Femtotesla nearly-quantum-noise-limited pulsed gradiometer at Earth-scale fields," Phys. Rev. Appl. **18**, L021001 (2022).
222. R. J. Cooper, D. W. Prescott, K. L. Sauer, *et al.*, "Intrinsic radio-frequency gradiometer," Phys. Rev. A **106**, 053113 (2022).
223. A. Jarmola, S. Lourette, V. M. Acosta, *et al.*, "Demonstration of diamond nuclear spin gyroscope," Sci. Adv. **7**, eabl3840 (2021).
224. G. Morigi, S. Franke-Arnold, and G.-L. Oppo, "Phase-dependent interaction in a four-level atomic configuration," Phys. Rev. A **66**, 053409 (2002).
225. D. Anderson, R. Sapiro, L. Gonçalves, *et al.*, "Optical radio-frequency phase measurement with an internal-state Rydberg atom interferometer," Phys. Rev. Appl. **17**, 044020 (2022).
226. S. Berweger, A. B. Artusio-Glimpse, A. P. Rotunno, *et al.*, "Closed-loop quantum interferometry for phase-resolved Rydberg-atom field sensing," Phys. Rev. Appl. **20**, 054009 (2023).
227. B. Kasza, S. Borówka, W. Wasilewski, *et al.*, "Atomic-optical interferometry in fractured loops: a general solution for Rydberg radio frequency receivers," Phys. Rev. A **111**, 053718 (2025).
228. S. Borówka, M. Mazelanik, W. Wasilewski, *et al.*, "Optically-biased Rydberg microwave receiver enabled by hybrid nonlinear interferometry," Nat. Commun. **16**, 8975 (2025).